Electronic Supplementary Information (ESI)

Two-dimensional g-C_3N_4: an ideal platform for examining facet selectivity of metal co-catalysts in photocatalysis

Song Bai, Xijun Wang, Canyu Hu, Maolin Xie, Jun Jiang* and Yujie Xiong*

Hefei National Laboratory for Physical Sciences at the Microscale, Collaborative Innovation Center of Chemistry for Energy Materials, and School of Chemistry and Materials Science, University of Science & Technology of China, Hefei, 230026, P.R. China.

E-mail: yjxiong@ustc.edu.cn, jiangj1@ustc.edu.cn

The first two authors contributed equally to this work.

Chemicals. K_2PdCl_4 (Aladdin, P106044) and poly(vinyl pyrrolidone) (PVP, M.W.≈29000, Aldrich, 234257) were purchased from Aladdin. All other chemicals were of analytical grade and purchased from Sinopharm Chemical Reagent Co., Ltd. The water used in all experiments was de-ionized. All chemicals were used as received without further purification.

Preparation of bulk g-C_3N_4 and C_3N_4 nanosheets. The bulk g-C_3N_4 was prepared by a modified method according to a previous paper.[S1] In a typical process, melamine was heated in air at 550°C for 4 h (ramp rate: 2°C/min; cooling rate: 1°C/min). The resultant yellow agglomerates were milled into g-C_3N_4 powder in a mortar. The C_3N_4 nanosheets were obtained by exfoliating the as-prepared bulk g-C_3N_4 powder in a mixed solvent of water and isopropanol (IPA). Specifically, 400.0 mg of g-C_3N_4 powder was dispersed in a 200-mL water-IPA mixed solvent (30 wt% IPA), and then sonicated for 10 h with a probe sonication (Scientz-IID, China). The formed suspension was centrifuged at 8,000 rpm for 10 min to remove aggregates. The product from the suspension was washed with water, collected by centrifugation at 15,000 rpm, and finally dried at 45°C. The obtained C_3N_4 nanosheets could be re-dispersed in various solutions for further use.

Synthesis of C_3N_4-Pd nanotetrahedrons. In a typical synthesis, K_2PdCl_4 (4.9 mg), $Na_2C_2O_4$ (50.3 mg) and PVP (8.3 mg) were dissolved in 5 mL of aqueous suspension containing g-C_3N_4 nanosheets, followed by the addition of 200-μL formaldehyde solution. The pH value of the solution was adjusted to 4 by adding drops of 1-M HCl solution. Subsequently the total volume of the solution was diluted to 7.5 mL with water. The solution was then transferred to a 10-mL Teflon-lined stainless steel autoclave and heated at 150°C for 2 h. After the autoclave had cooled down to room temperature, the resultant product was separated by centrifugation, and washed with acetone once, water three times and ethanol two times. The C_3N_4-Pd nanotetrahedrons with different Pd loading amounts were obtained by altering the concentrations of C_3N_4 in the aqueous suspension for the synthesis.

Synthesis of C_3N_4-Pd nanocubes. In a typical synthesis, K_2PdCl_4 (4.9 mg), KBr (89.3 mg) and PVP (25.0 mg) were dissolved in 5 mL of aqueous suspension containing g-C_3N_4 nanosheets, followed by the addition of 150-μL KI aqueous solution (0.01-M). The pH value of the solution was adjusted to 3 by adding drops of 1-M HCl solution. Subsequently the total volume of the solution was diluted to 7.5 mL with water. The solution was then transferred to a 10-mL Teflon-lined stainless steel autoclave and heated at 150°C for 3 h. After the autoclave had cooled down to room temperature, the resultant product was separated by centrifugation, and washed with acetone once, water three times and ethanol two times. The C_3N_4-Pd nanocubes with different Pd loading amounts were obtained by altering the concentrations of C_3N_4 in the aqueous suspension for the synthesis.

Sample characterizations: X-ray powder diffraction (XRD) patterns were recorded by using a Philips X'Pert Pro Super X-ray diffractometer with Cu-Kα radiation (λ = 1.54178 Å). Transmission electron microscopy (TEM), high-resolution TEM (HRTEM), scanning transmission electron microscopy (STEM) images, and energy-dispersive spectroscopy (EDS) mapping profiles were taken on a JEOL JEM-2100F field-emission high-resolution transmission electron microscope operated at an acceleration voltage of 200 kV. Atomic force microscopy (AFM) measurements were performed with a Veeco DI Nanoscope MultiMode V system. Photoluminescence (PL) measurements were recorded on a Jobin Yvon Horiba Fluorolog-3-Tau Spectrofluorometer. X-ray photoelectron spectra (XPS) were collected on an ESCALab 250 X-ray photoelectron spectrometer, using nonmonochromatized Al-Kα X-ray as the excitation source. The concentrations of Pd were measured with a Thermo Scientific PlasmaQuad 3 inductively-coupled plasma mass spectrometry (ICP-MS) after dissolving the particles with a mixture of HCl and HNO_3 (3:1, volume ratio). UV-vis diffuse reflectance data were recorded in the spectral region of 250–1000 nm with a Shimadzu SolidSpec-3700 spectrophotometer. The Fourier transform infrared (FT-IR) measurements were carried out on a Nicolet 8700 FT-IR spectrometer in a KBr pellet, scanning from 4000 to 500 cm^{-1} at room temperature.

Photoelectrochemical measurements: The as-synthesized products containing 2-mg C_3N_4 were dispersed in 1 mL of ethanol, which were then uniformly spincoated onto a 2.5 cm × 2.5 cm indium tin oxide (ITO)-coated glass by a spincoater (SC-1B, China). Subsequently, the ITO-coated glass was heated at 80°C in a vacuum oven for 1 h. The weight of C_3N_4 in the hybrid structures was determined by measuring the concentrations of the Pd components with the ICP-MS.

The photocurrents were measured on a CHI 660D electrochemical station (Shanghai Chenhua, China) in ambient condition, under irradiation of a 300-W Xe lamp (Solaredge 700, China) with a 400-nm long-wave-pass cut-off filter (λ>400 nm). The power density of light was measured to be 100 mW/cm^2. A standard three-electrode setup was used with the ITO-coated glass as a photoelectrode, a Pt foil as a counter electrode, and a Ag/AgCl electrode as a reference electrode. The three electrodes were inserted in a quartz cell filled with 0.5-M Na_2SO_4 electrolyte (100 mL, pH = 6.6). The Na_2SO_4 electrolyte was purged with Ar for 30 min prior to the measurement. The photoresponse of the prepared photoelectrodes was operated by sweeping the potential from 0.1 to 0.7 V (*vs.* Ag/AgCl) at a sweep rate of 10 mV/s under chopped irradiation (light on/off cycles: 6 s). The electrochemical impedance spectroscopy (EIS) was carried out in the frequency range of 10^{-2} to 10^5 Hz with an AC voltage amplitude of 10 mV at a bias potential of 0.6 V *vs.* Ag/AgCl in a 0.5-M Na_2SO_4 solution under light illumination.

Photocatalytic measurements: To investigate the photocatalytic activities of C_3N_4-based catalysts for CO_2 reduction, 10 mg of photocatalysts was dispersed on a porous catalyst holder made of quartz sand in the upper region of a reactor. The Pd loading amounts were determined by measuring the concentrations of the Pd components with the ICP-MS. The reactor was home-made with stainless steel and quartz tube. The set-up of photocatalytic system is illustrated in Fig. S22. In the reactor, the quartz tube has a length of 340 mm and an outer diameter of 20 mm. The total volume of the reactor is about 100 mL. Liquid water with a volume of 3 mL was pre-charged in the bottom of the reactor, and the catalysts were not immersed into the liquid water but surrounded by H_2O vapor and CO_2. The reactor loaded with catalysts was first purged with CO_2 at 50 mL/min for 20 min. Subsequently, the valves were closed, and the pressure of CO_2

was regulated to 0.15 MPa. The light-irradiation experiment was performed by using a 300W Xe lamp with a 400-nm long-wave-pass cut-off filter (λ>400 nm). The power density of light was measured to be 100 mW/cm^2. The photocatalytic reaction was typically performed for 4 h. The amount of gas and liquid products evolved were all determined using gas chromatography (GC, 7890A, Ar carrier, Agilent). The gas products were separated by a HP-5 column. Specifically, H_2 and CH_4 were determined using a thermal conductivity detector (TCD) and a flame ionization detector (FID), respectively. The CO was converted to CH_4 by a methanation reactor and then analyzed by the FID. C_2H_5OH in liquid phase was determined by the FID with a DB-FFAP column. The formation of O_2 was also observed on the TCD during the photocatalytic reduction of CO_2 with H_2O. Other possible products such as C_2H_4, C_2H_6, HCOOH, HCHO and CH_3OH were not detected in our reactions. When in the dark, no product was detected for all the catalysts. Three replicates were collected for each catalyst with relative error < 10%.

For the measurements of CO_2 reduction, the catalysts were carefully pretreated to remove any possible organic contaminations prior to the tests: (1) the samples were baked in a vacuum oven at 150°C for 24 h to remove residues of alcohol solvents and other organic agents; (2) they were loaded in the reactor and irradiated exposed to H_2O vapor in 0.15-MPa Ar, which can effectively eliminate trace carbon residues from our samples and reactor.[S2] Further, the pretreated samples were tested in 0.15-MPa fresh Ar in the absence of CO_2 but in the presence of H_2O, which showed no activity to generate carbon products and thus confirmed that our following measurements were free of any carbon contaminants. We have also performed FT-IR, XPS and blank electrochemical cyclic voltammetry (CV) tests to confirm the cleanliness of sample surface. The CO_2 source was also analyzed by the GC FID, and the resulted signals were used as a blank deducted from our photocatalytic data, avoiding any influence from the impurities in the CO_2 source.

The numbers of electrons required to produce H_2, CO, C_2H_5OH, and CH_4 are shown in the following equations (eq. (1)–(4)).

$$2H^+ + 2e^- \rightarrow H_2 \qquad (1)$$

$$CO_2 + 2H^+ + 2e^- \rightarrow CO + H_2O \qquad (2)$$

$2CO_2 + 12H^+ + 12e^- \rightarrow C_2H_5OH + 3H_2O$ (3)

$CO_2 + 8H^+ + 8e^- \rightarrow CH_4 + 2H_2O$ (4)

The reduction selectivity for CO_2 to H_2O was evaluated based on the required electrons using the follow equation:

Selectivity (%) = $[2v(CO) + 12v(C_2H_5OH) + 8v(CH_4)]/[2v(CO) + 12v(C_2H_5OH) + 8v(CH_4) + 2v(H_2)] \times 100\%$

where $v(H_2)$, $v(CO)$, $v(C_2H_5OH)$ and $v(CH_4)$ stand for the formation rates for H_2, CO, C_2H_5OH, and CH_4.

Computational methods: We used the Vienna *ab initio* Simulation (VASP) package to optimize the geometric structures and simulate the electronic structures of various systems.[S3] Calculations were performed at the spin-polarized density functional theory (DFT) level using frozen-core all-electron projector augmented wave (PAW) model with the generalized gradient approximation (GGA) and Perdew-Burke-Ernzerhof (PBE) functions. An energy cutoff of 400 eV was used for the plane-wave expansion of the electronic wave function. The force and energy convergence criterion was set to 0.01 eV/Å and 10^{-5} eV, respectively. A C_3N_4 plane containing 3 × 3 unit cells was used as the substrate, being interfaced with the structure of a 3 × 3 Pd slab with five layers for both Pd{100} and Pd{111} (which are chosen in considerations of the small Pd particle sizes 4-6 nm that may induce quantum effect). The 8 × 8 × 1 *k*-points test was performed for the first Brillouin zone using the gamma center scheme. There were 7 different interface structures being employed to model the hybrid configurations for both C_3N_4-Pd{100} and C_3N_4-Pd{111}, and projected density of states (PDOS) was calculated by combining contributions from different positions regarding to their distribution probability. The position of a single CO_2 or H_2O molecule on the Pd{100} and Pd{111} above was optimized by the VASP program to obtain adsorption energy and determine the most favorable adsorption structure.

Based on the optimized structure from the VASP calculations, the CO_2 or H_2O on Pd{100} or Pd{111} with 1 molecule and 1 Pd layer involved was extracted. Then the Gaussian09 program

was employed to simulate potential energy surface along the variation of C-O or O-H bonding, to obtain the activation energy barrier for CO_2 or H_2O reduction.[S4]

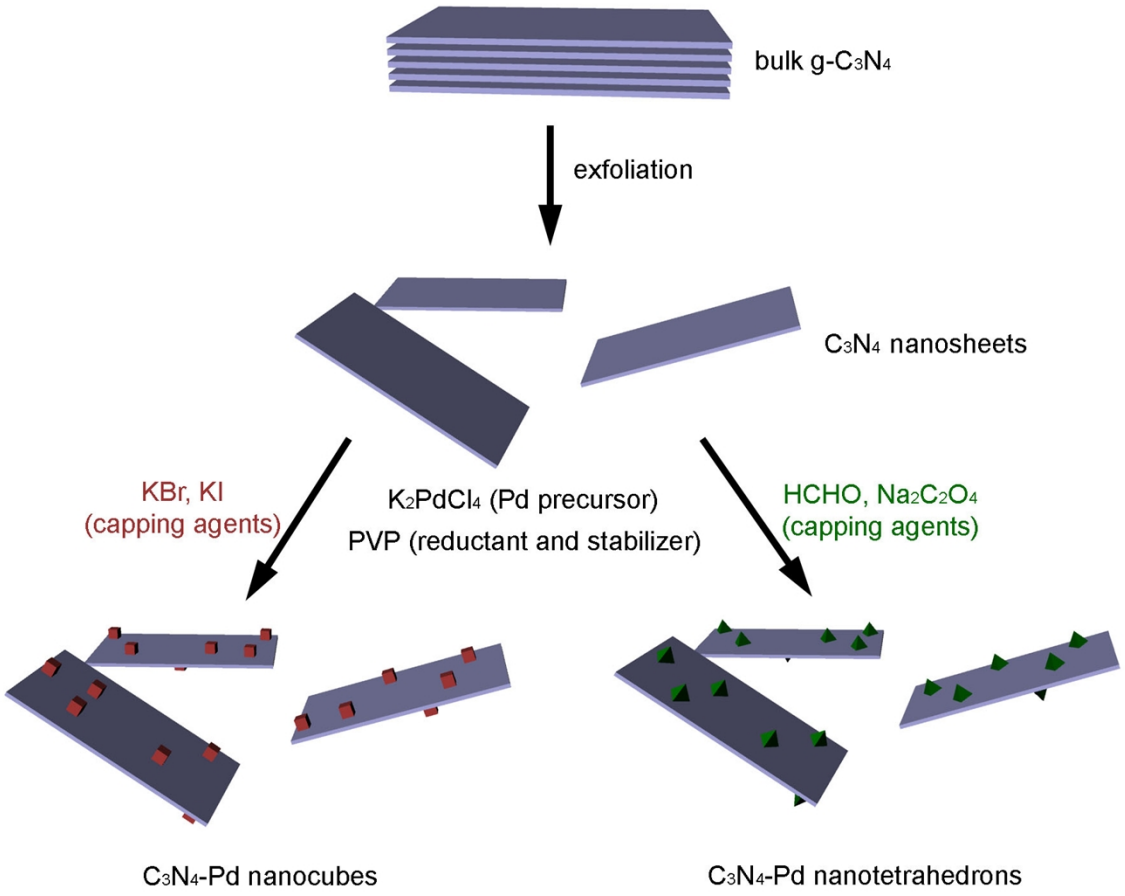

Fig. S1 Schematic illustrating the synthetic approach to C_3N_4-Pd hybrid structures. In our synthesis, PVP is employed as a dual-function agent.[S5] The hydroxyl end groups of PVP can reduce Pd precursor to zero-valent Pd. On the other hand, the presence of PVP can stabilize the yielded Pd nanocrystals and prevent their aggregation, ensuring the uniform dispersion of Pd on C_3N_4 nanosheets.

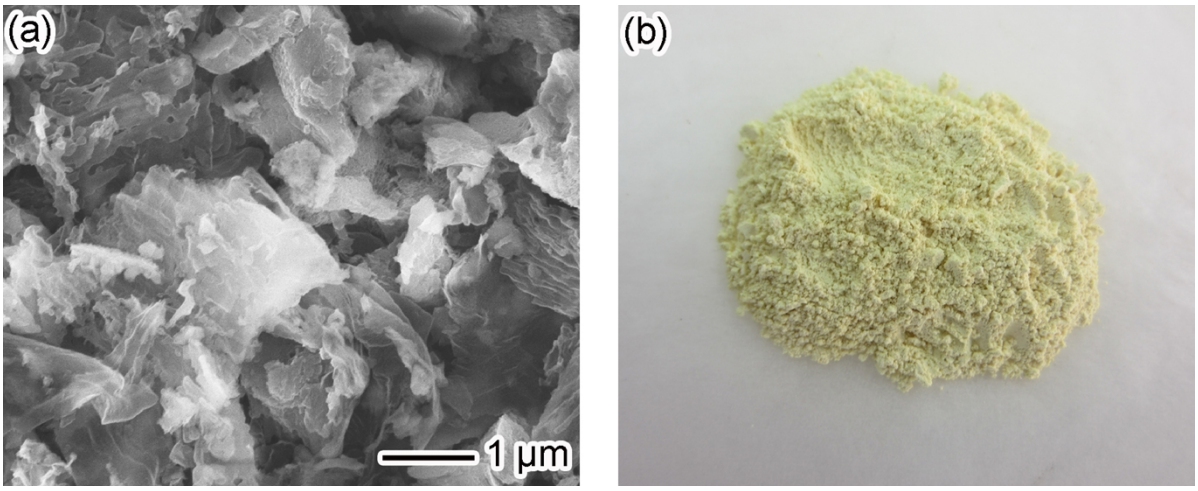

Fig. S2 (a) SEM image and (b) photograph of bulk g-C_3N_4 powder.

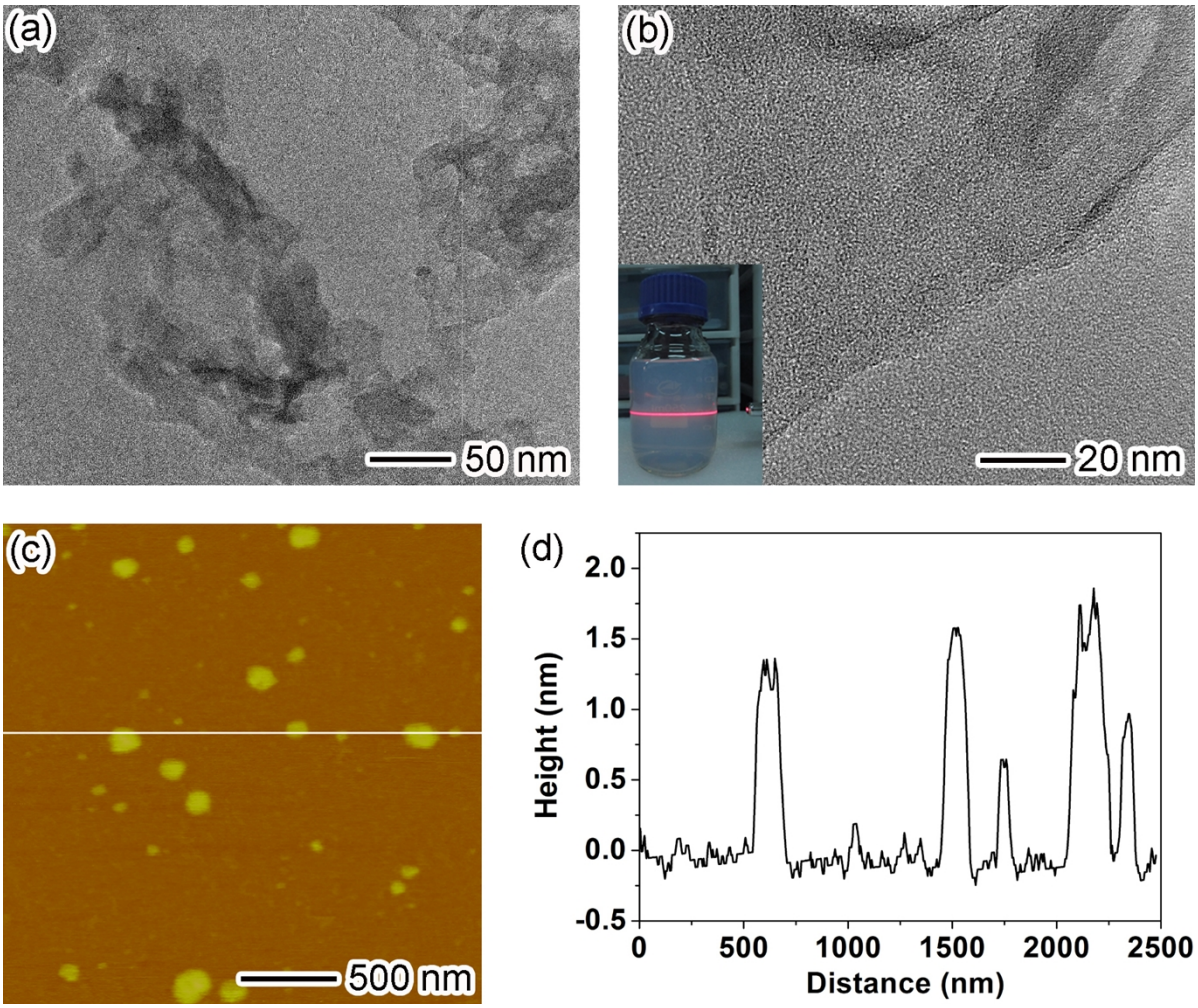

Fig. S3 (a, b) TEM images of C_3N_4 nanosheets. (c) AFM image and (d) the corresponding height profile of C_3N_4 nanosheets. The inset of (b) exhibits the typical Tyndall effect of the corresponding C_3N_4 nanosheets dispersed in water.

The thickness of the C_3N_4 nanosheets is about 2 nm. According to the XRD pattern ((002) peak at 27.4° in Fig. S5), the interlayer spacing of g-C_3N_4 is about 0.326 nm.[S6] Thus the nanosheets should contain about six C_3N_4 layers.

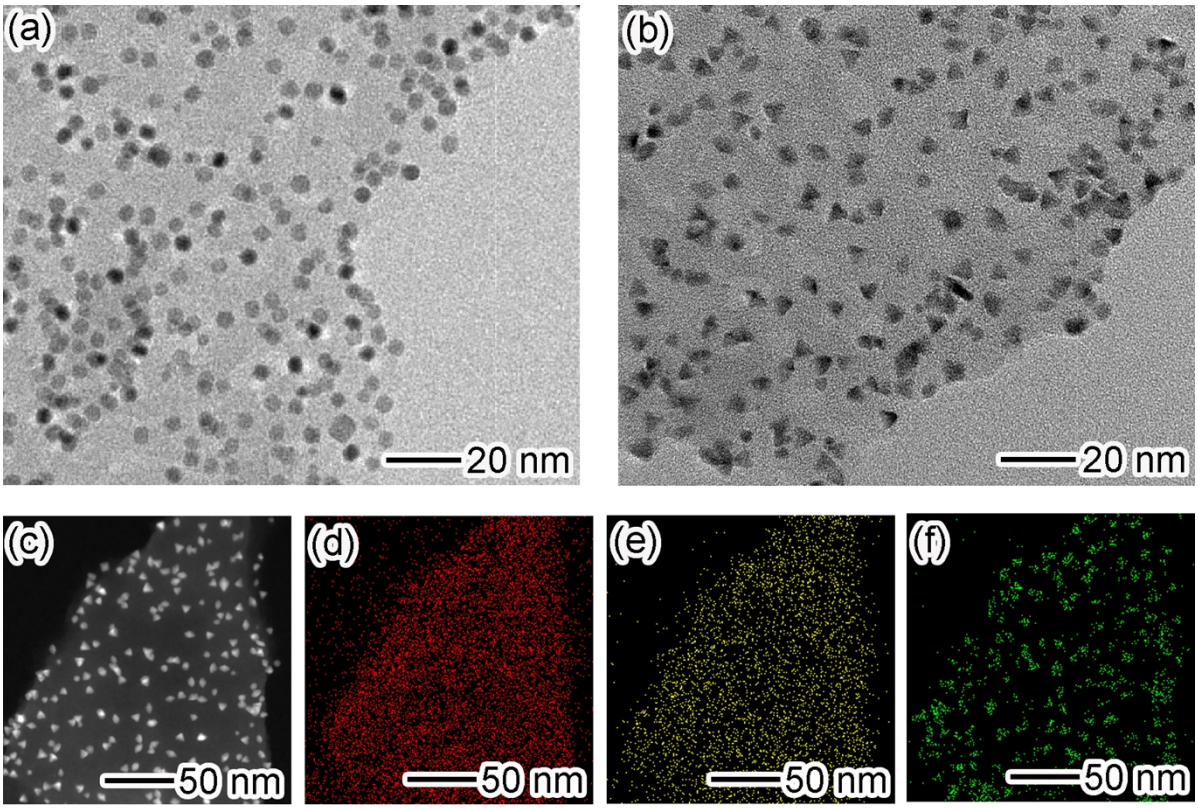

Fig. S4 Representative TEM images of (a) C_3N_4-Pd nanocubes (NCs) with Pd{100} facets and (b) C_3N_4-Pd nanotetrahedrons (NTs) with Pd{111} facets. (c) STEM image of C_3N_4-Pd NTs. EDS mapping profiles of elements in the sample c: (d) C, (e) N, and (f) Pd, respectively. The STEM and EDS mapping analyses further confirm the compositions of loaded Pd and C_3N_4 supports.

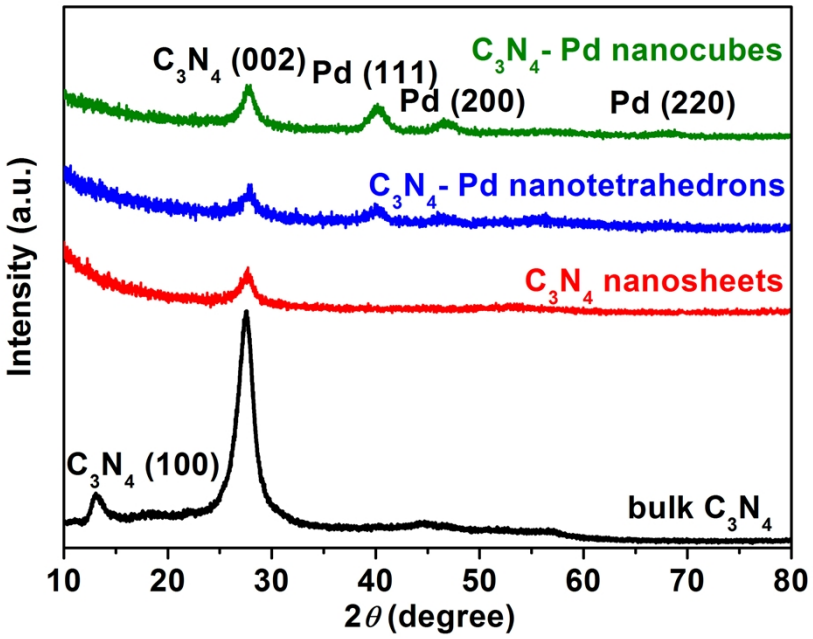

Fig. S5 XRD patterns of bulk C_3N_4, C_3N_4 nanosheets, C_3N_4-Pd nanotetrahedrons and C_3N_4-Pd nanocubes.

The XRD pattern of bulk C_3N_4 shows two diffraction peaks at $2\theta = 13.1^o$ and 27.4^o, which match well with the (100) and (002) crystal planes of g-C_3N_4, respectively. The (100) peak represents the in-planar repeating tri-*s*-triazine unit, while the strong (002) peak is the characteristic interlayer stacking reflection of the conjugated aromatic system.[S6] As for C_3N_4 nanosheets, the intensity of (002) peak significantly decreases, indicating that the layered C_3N_4 has been fully exfolicated.[S7] In comparison with C_3N_4 nanosheets, both C_3N_4-Pd nanocubes and C_3N_4-Pd nanotetrahedrons show additional peaks, which can all be indexed to face-centered cubic (*fcc*) Pd (JCPDS No. 65-2867).

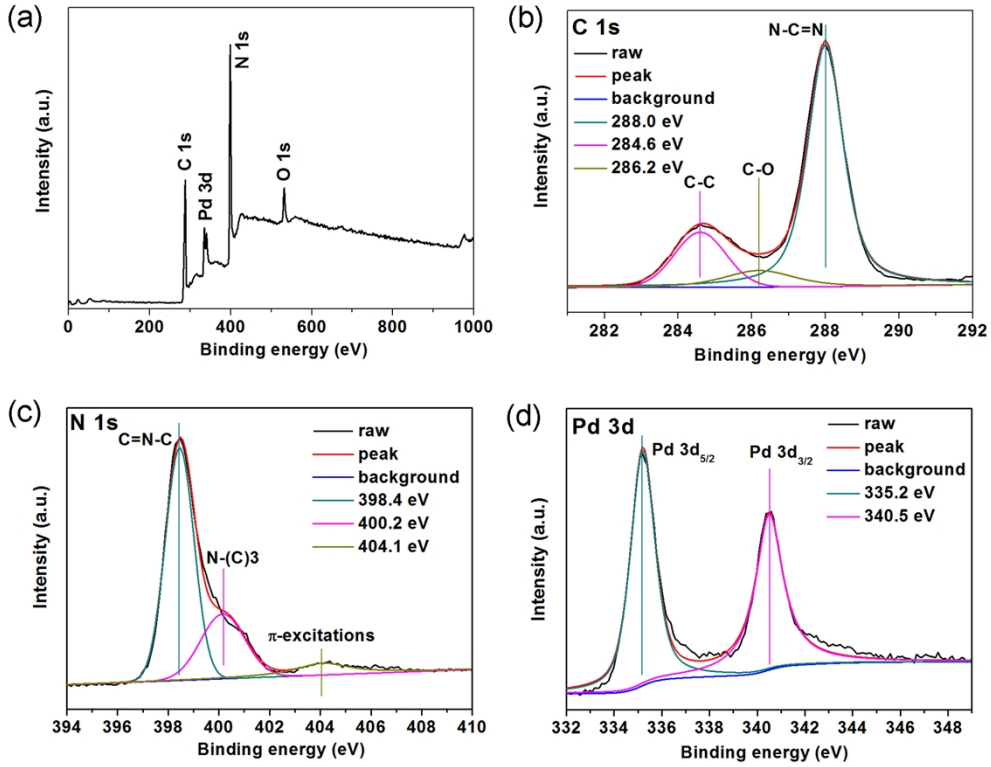

Fig. S6 XPS spectra of C_3N_4-Pd nanotetrahedrons: (a) survey spectrum, (b) C1s, (c) N1s and (d) Pd3d high-resolution spectra.

The survey XPS spectrum (Fig. S6a) indicates the C, N, Pd and O peaks in C_3N_4-Pd hybrid structures. The O could be ascribed to the C-O stemming from the incompletely reacted oxygen-containing intermediates during the synthesis of g-C_3N_4 as well as the small amount of absorbed H_2O and IPA in the exfoliation process.[S1,S8] The high-resolution spectrum of C1s (Fig. S6b) can be deconvoluted into three peaks at 288.0 eV, 284.6 eV and 286.2 eV, corresponding to sp^2-bonded aromatic structure (N-C=N), graphitc carbon (C-C), and residual C–O, respectively. Meanwhile, the high-resolution spectrum of N1s (Fig. S6c) can also be divided into three peaks at 398.4 eV, 400.2 eV, and 404.1 eV, attributed to sp^2-hybridized aromatic N (C=N-C), tertiary N bonded to carbon atoms [N-$(C)_3$], and π-excitations, respectively.[S8] The two peaks in Pd3d (Fig. S6d) located at 335.2 eV and 340.5 eV are assigned to $Pd3d_{5/2}$ and $Pd3d_{3/2}$, respectively, which are in good agreement with the zero valence of Pd.

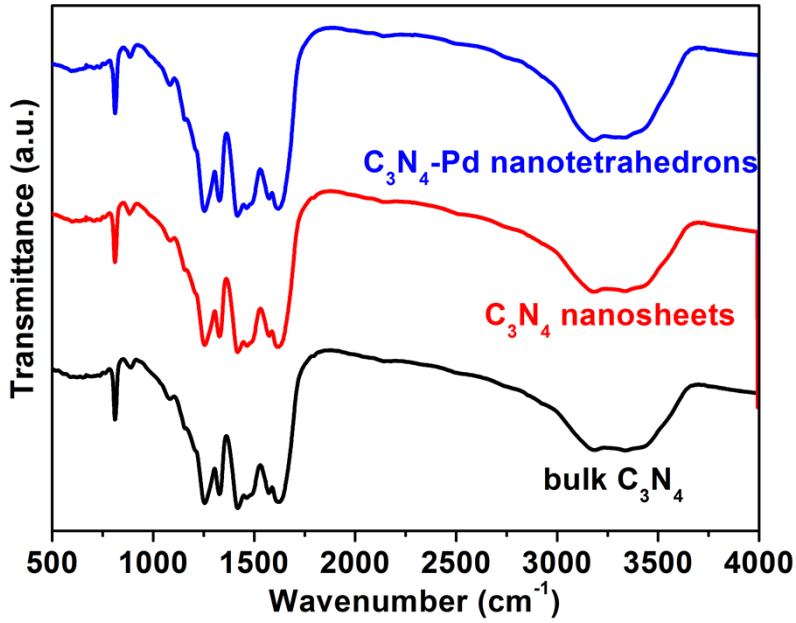

Fig. S7 FT-IR spectra of bulk C_3N_4, C_3N_4 nanosheets and C_3N_4-Pd nanotetrahedrons.

In the FT-IR spectrum of bulk C_3N_4, the peak at 810 cm^{-1} originates from the characteristic breathing mode of the s-triazine ring. The peaks between 1000 and 1800 cm^{-1} correspond to the stretching vibrations of C=N and C-N heterocycles, while the board peaks between 3000 and 3600 cm^{-1} are attributed to the N-H stretching.[S1,S7,S9] The FT-IR features are unchanged when the bulk C_3N_4 is exfoliated into nanosheets and further loaded with Pd.

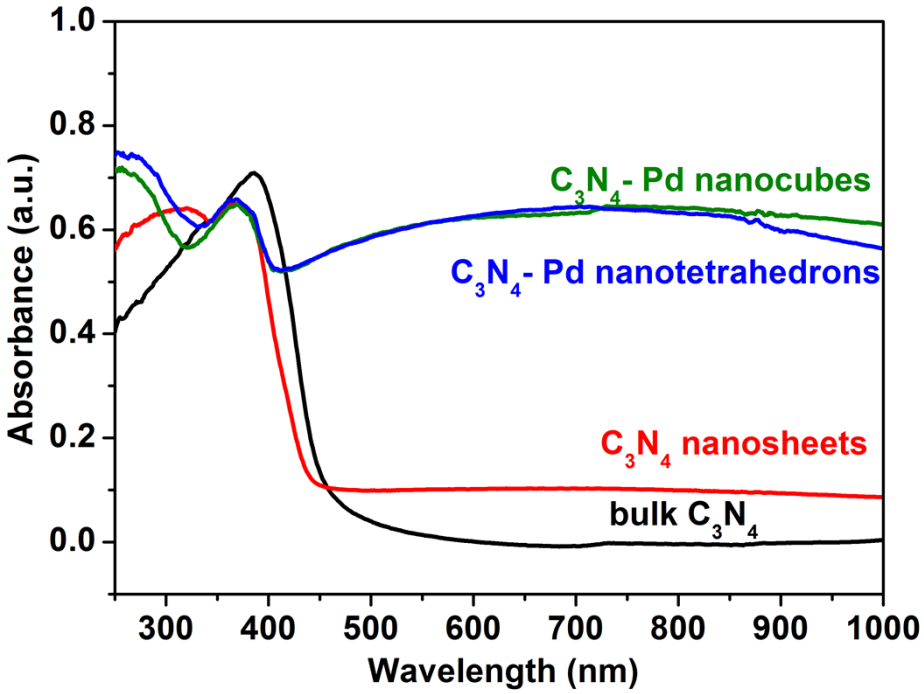

Fig. S8 UV-vis diffuse reflectance spectra of bulk C_3N_4, C_3N_4 nanosheets, C_3N_4-Pd nanotetrahedrons and C_3N_4-Pd nanocubes.

From the spectra, the bandgap of bulk C_3N_4 is estimated to be 2.64 eV. As for g-C_3N_4 nanosheets, the bandgap is increased to 2.70 eV, which is consistent with the previous report.[S1] With Pd nanocubes and nanotetrahedrons deposited, the bandgap of g-C_3N_4 has not been changed.

Note that the peaks in the UV region (<350 nm) should be assigned to the localized surface plasmon resonance (LSPR) of Pd.[S10] On the other hand, the C_3N_4-supported Pd nanoparticles are closely packed, resulting in the significantly high scattering at long wavelengths (from 420 to 1000 nm).[S11]

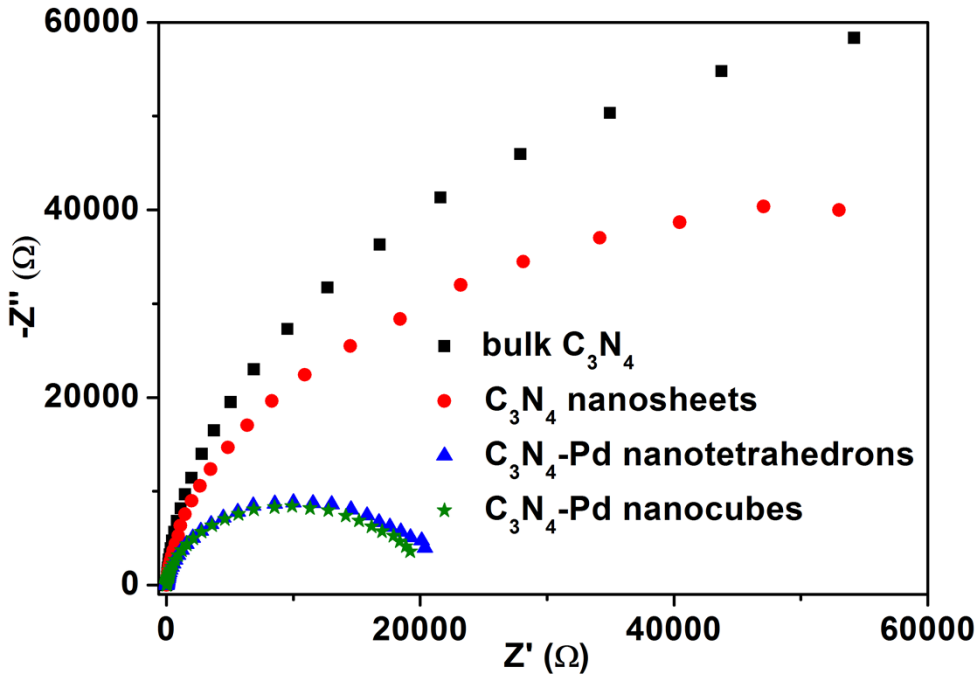

Fig. S9 EIS Nyquist plots of the bulk C_3N_4, C_3N_4 nanosheets, C_3N_4-Pd nanotetrahedrons and C_3N_4-Pd nanocubes electrodes at 0.6 V *vs.* Ag/AgCl. Pd loading amounts for the nanocubes and nanotetrahedrons are 5.7 wt% and 5.8 wt%, respectively.

In the EIS spectra (presented as Nyquist plots), the radii of C_3N_4-Pd hybrid structures are much smaller than those of bulk C_3N_4 and C_3N_4 nanosheets, showing lower charge-transfer resistance.[S7] It indicates the improved separation of photogenerated electron-hole pairs in the hybrid structures, which is consistent with the results of photocurrent tests. On the other hand, the comparable resistance of the two C_3N_4-Pd structures also confirms their equivalent charge-transfer efficiency.

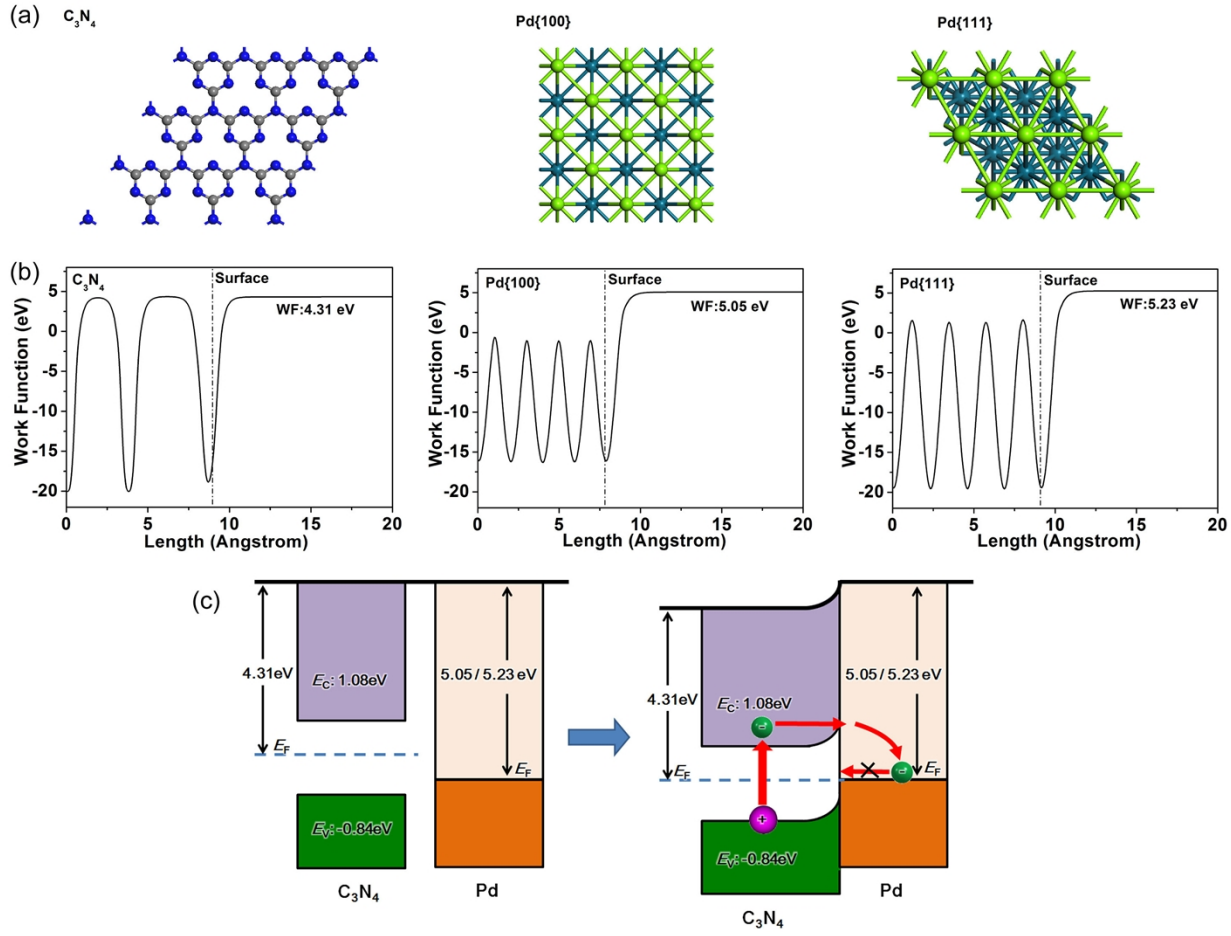

Fig. S10 (a) Model systems and (b) computed potential line-ups with work function values for C_3N_4, Pd{100} and Pd{111} (from left to right), respectively. (c) Energy level lineup diagrams for C_3N_4 and Pd before and after interfacing showing the conduction band (E_c), valence band (E_v) and Fermi levels (E_f) responsible for electron transfer, based on the first-principles calculation results.

Note that DFT calculations normally underestimate the gap value of C_3N_4 (2.7 eV as reported in experiments), but yet give accurate charge density distributions crucial to charge transfer and molecular interactions.[S12]

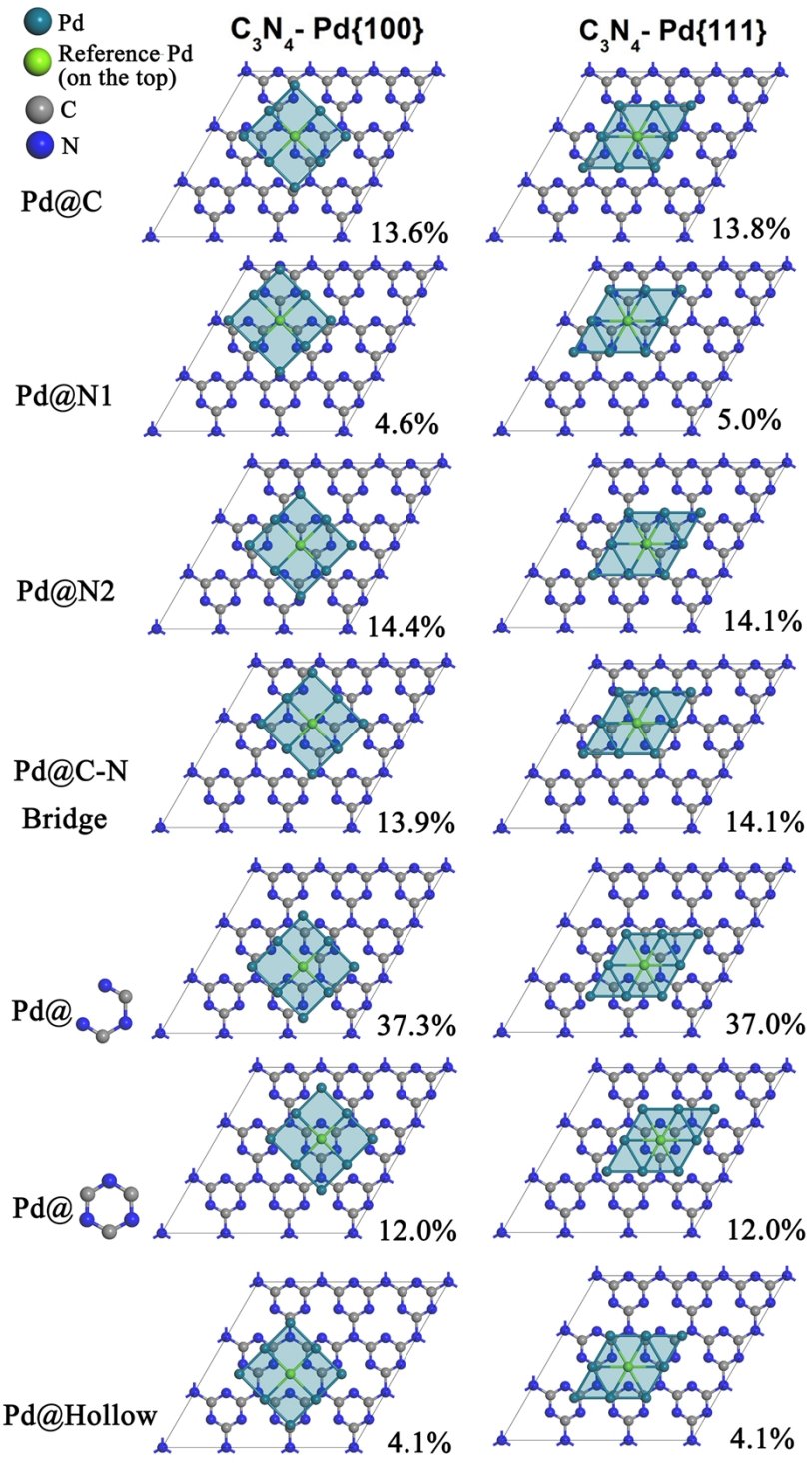

Fig. S11 Various interfacing configurations at the C_3N_4-Pd{100} and C_3N_4-Pd{111} interface, together with the content fractions of distribution probability for each configuration.

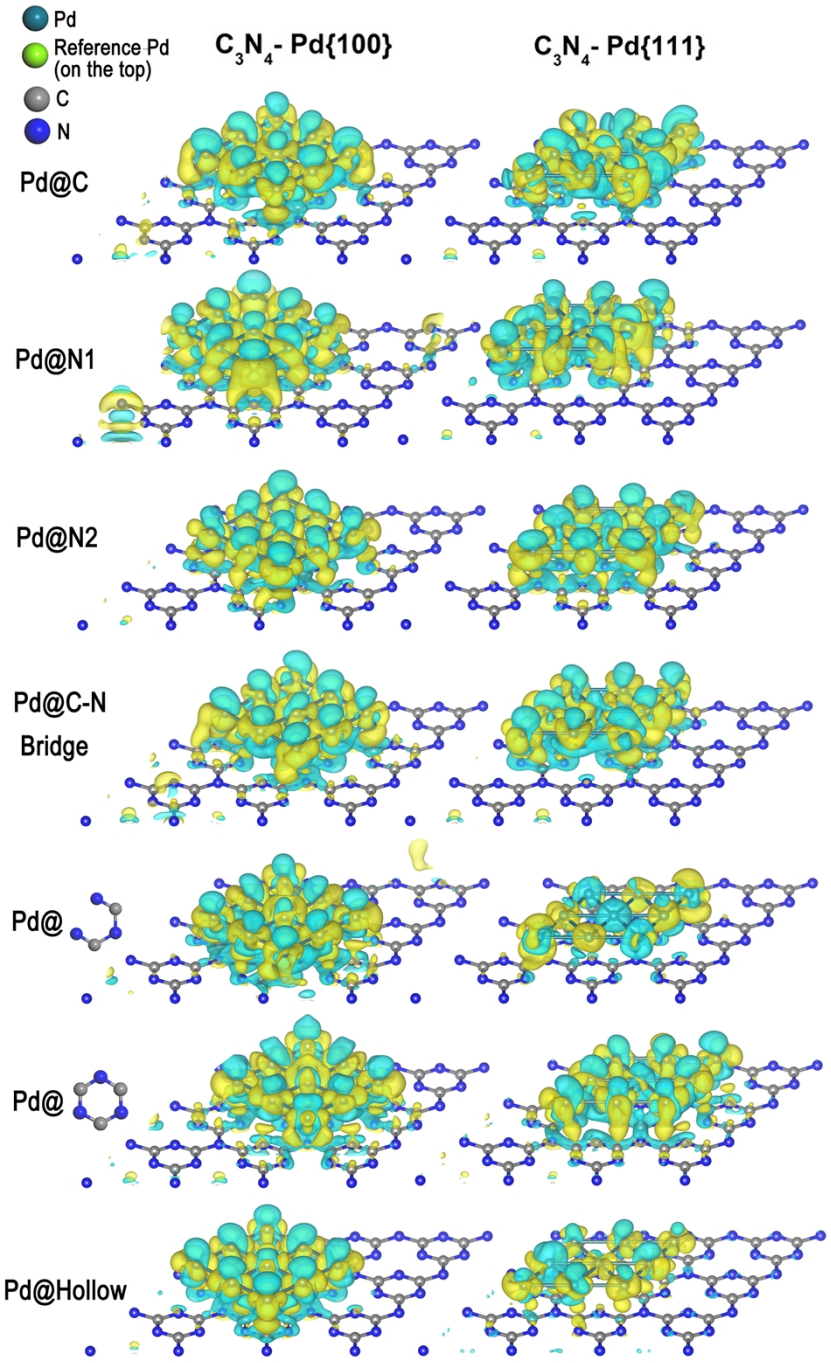

Fig. S12 Computed difference charge density (with the charges of the isolated C_3N_4 and metal crystal structures subtracted from that of the coupled system) spatial distributions for various interfacing configurations at the C_3N_4-Pd{100} and C_3N_4-Pd{111} interface. Here olive and cyan colors represent positive and negative signals (i.e., more and less charges induced by couplings), respectively.

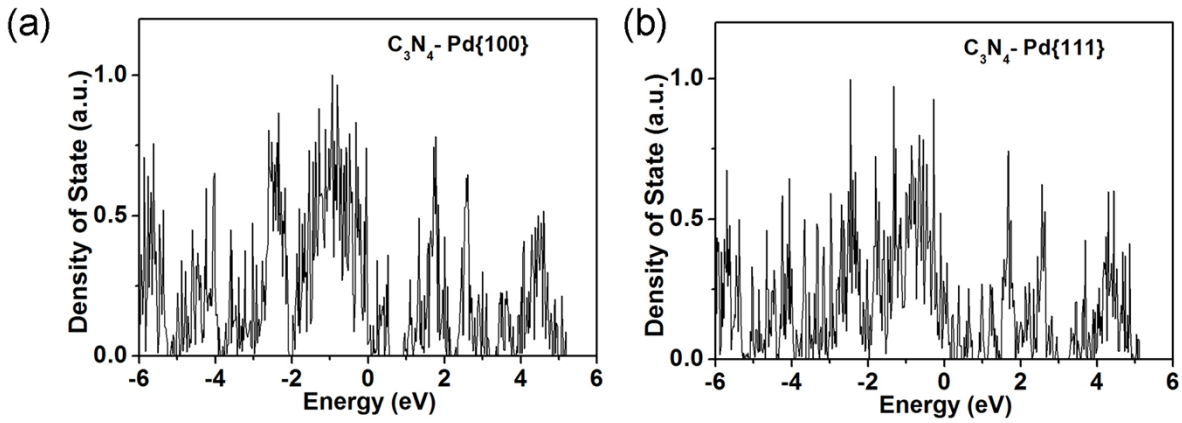

Fig. S13 Calculated PDOS of (a) C_3N_4-Pd{100} and (b) C_3N_4-Pd{111} by combining the contributions from various interfacing configurations regarding to their distribution probabilities.

The interfacing of C_3N_4 with Pd metal has been examined, which turns out to have seven contact configurations. The simulation reveals that the probability of each configuration has mostly similar content fraction for Pd{100} and Pd{111} (ESI,† Fig. S11). Furthermore, they exhibit similar coupling-induced difference charge density distributions at the interface (ESI,† Fig. S12), owing to the unique conjugated structure of C_3N_4. It is thus natural to obtain nearly identical projected density of states (PDOS) for C_3N_4 interfacing with Pd{100}/Pd{111} facets when combining the contributions from various contact cases (ESI,† Fig. S13). Basically, the coupling and hybridization of C_3N_4-Pd electronic structures revealed by the PDOS reflect the probability of interfacial charge transfer. As a result, these simulations together with the experimental findings above clearly show that the charge transfer behavior is not affected by altering the surface facets of Pd co-catalysts.

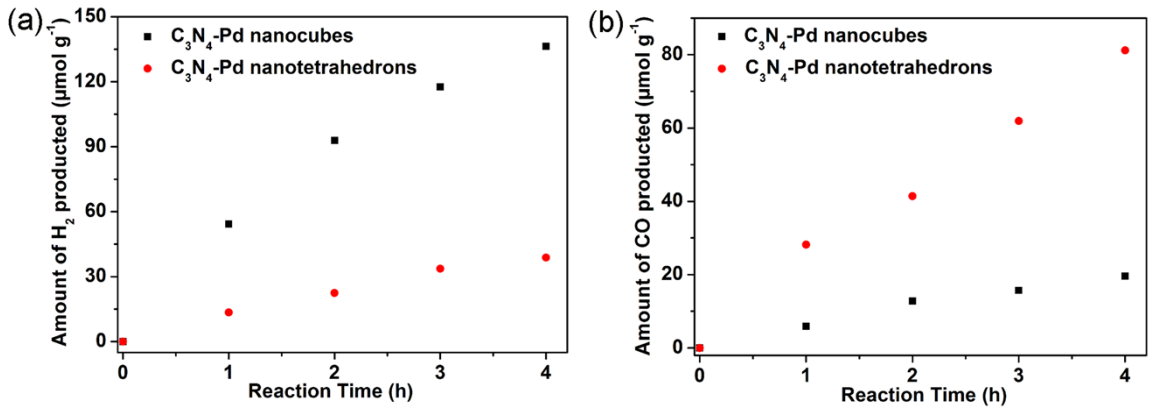

Fig. S14 (a) H_2 and (b) CO production as function of reaction time over the sample of C_3N_4-Pd nanocubes and C_3N_4-Pd nanotetrahedrons under visible light irradiation. Pd loading amounts for the nanocubes and nanotetrahedrons are 5.7 wt% and 5.8 wt%, respectively.

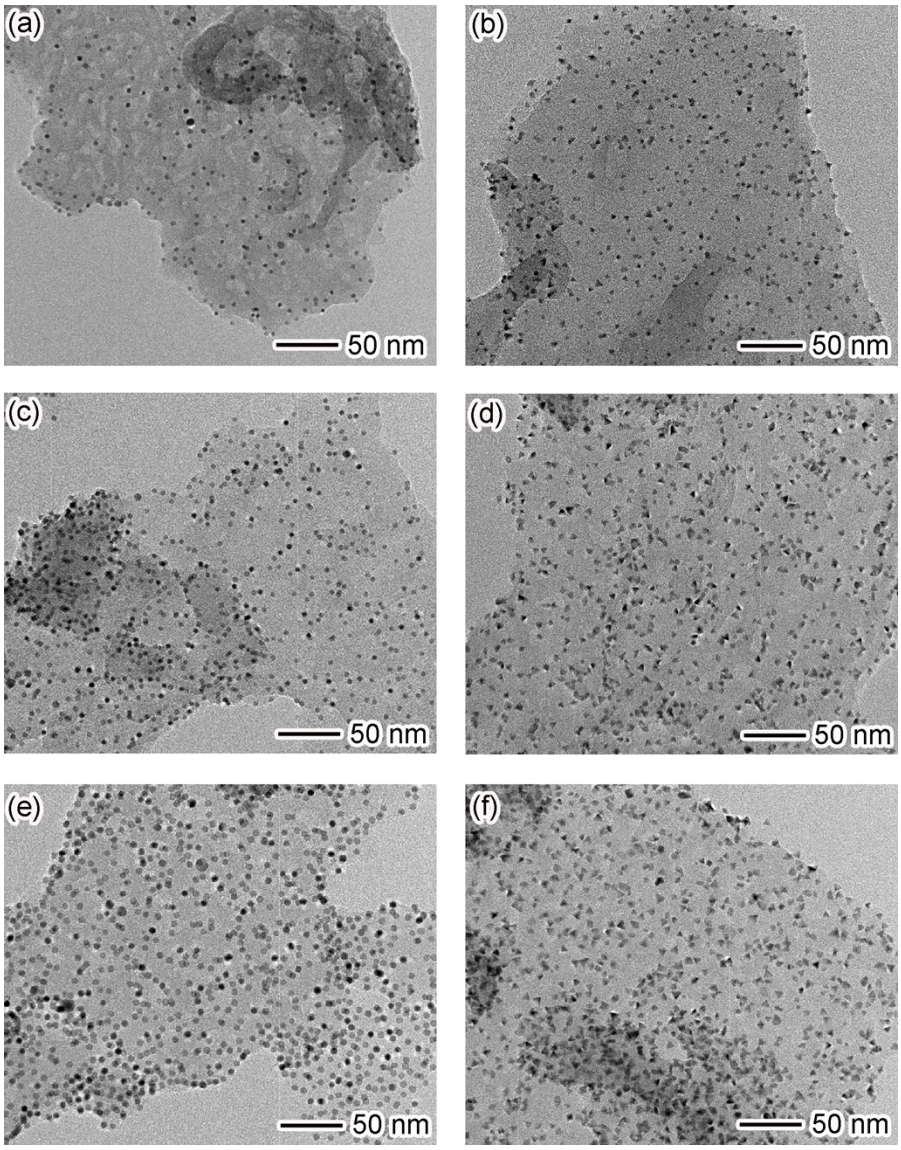

Fig. S15 TEM images of C_3N_4-Pd hybrid structures with different Pd loading amounts and surface facets: (a) nanocubes (2.9 wt%), (b) nanotetrahedrons (3.1 wt%), (c) nanocubes (5.7 wt%), (d) nanotetrahedrons (5.8 wt%), (e) nanocubes (11.9 wt%) and (f) nanotetrahedrons (11.6 wt%).

The different Pd loading amounts were controlled by altering the concentrations of C_3N_4 in the aqueous suspension for the synthesis. With the increase of the C_3N_4 amount in the reaction system, both the size and distribution density of Pd nanocrystals decrease. It indicates the

increased nucleation sites for Pd in the case of high C_3N_4 concentration, further verifying the *in-situ* nucleation and growth modes of Pd on the C_3N_4.

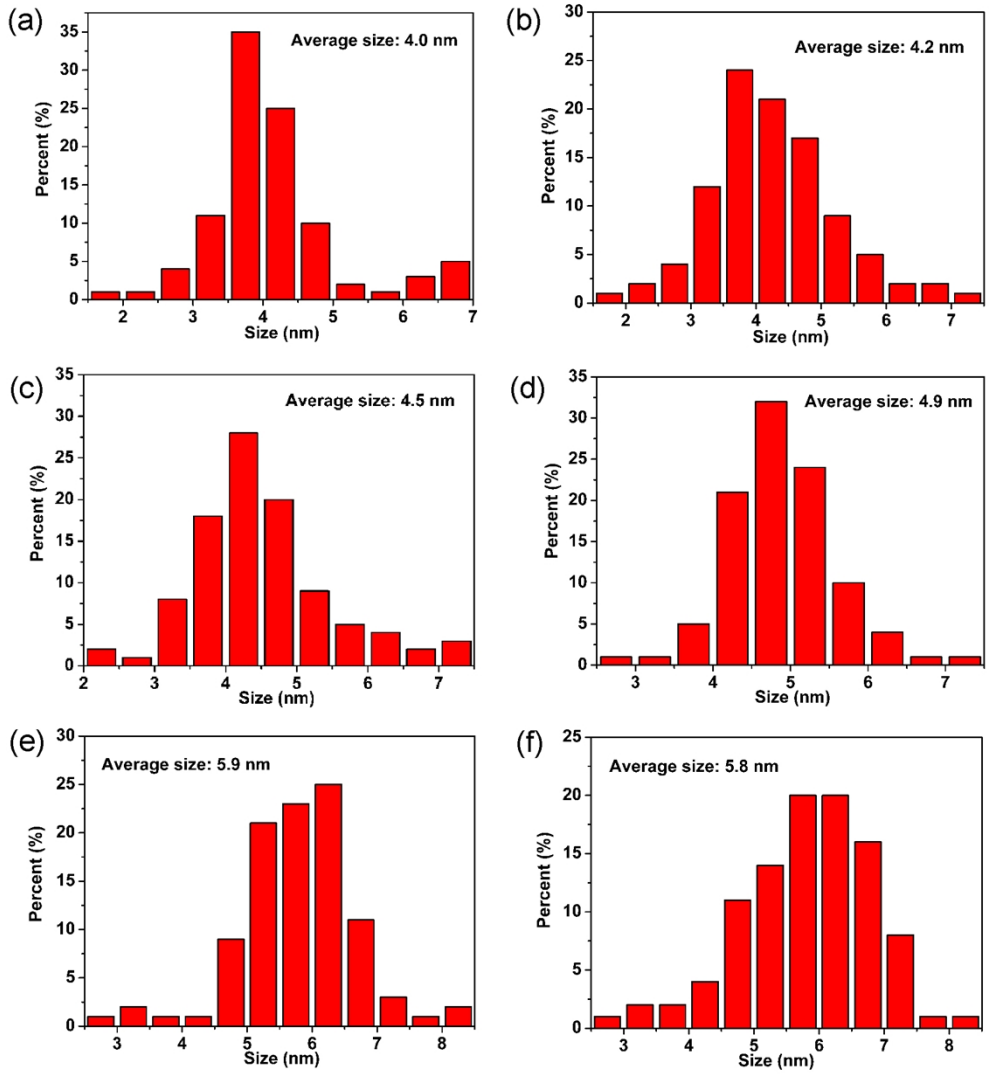

Fig. S16 Size distribution histograms of the as-prepared Pd nanocubes and nanotetrahedrons on the C_3N_4 nanosheets: (a) nanocubes (2.9 wt%), (b) nanotetrahedrons (3.1 wt%), (c) nanocubes (5.7 wt%), (d) nanotetrahedrons (5.8 wt%), (e) nanocubes (11.9 wt%) and (f) nanotetrahedrons (11.6 wt%). The sizes were measured according to the edge lengths of the cubic and tetrahedral nanocrystals, respectively.

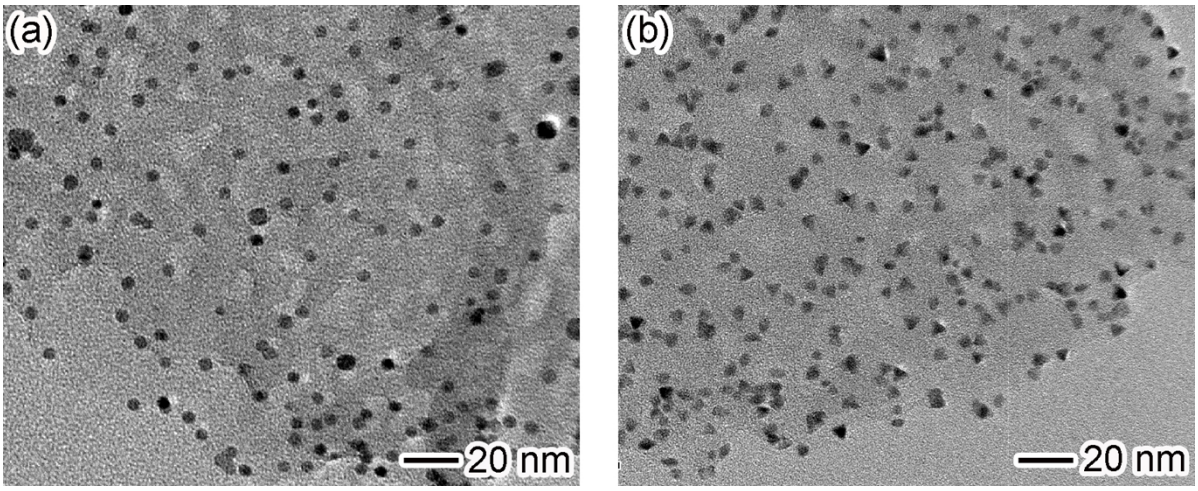

Fig. S17 TEM images of (a) C_3N_4-Pd nanocubes (5.7 wt% Pd) and (b) C_3N_4-Pd nanotetrahedrons (5.8 wt% Pd) after three photocatalytic reactions.

There was no obvious morphological change in the Pd nanocubes and nanotetrahedrons after three photocatalytic reactions, indicating the high catalytic stability of both photocatalysts. Moreover, neither Pd nanocubes nor nanotetrahedrons were found to fall off from the C_3N_4 nanosheets, further confirming their intimate contact with the C_3N_4.

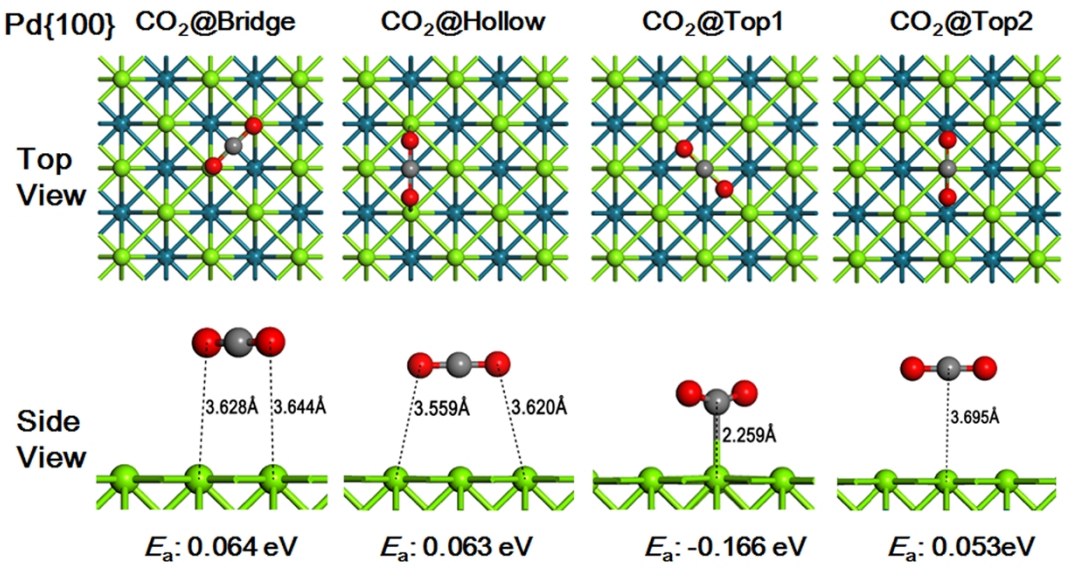

Fig. S18 Adsorption configurations for CO_2 to Pd{100} surface together with corresponding adsorption energy E_a, based on geometry optimization simulations.

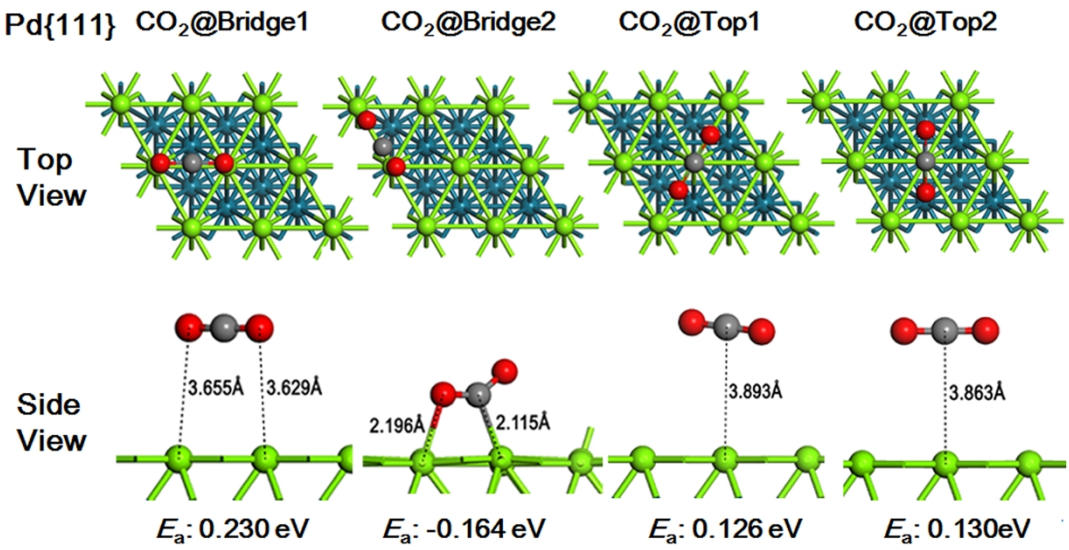

Fig. S19 Adsorption configurations for CO_2 to Pd{111} surface together with corresponding adsorption energy E_a, based on geometry optimization simulations.

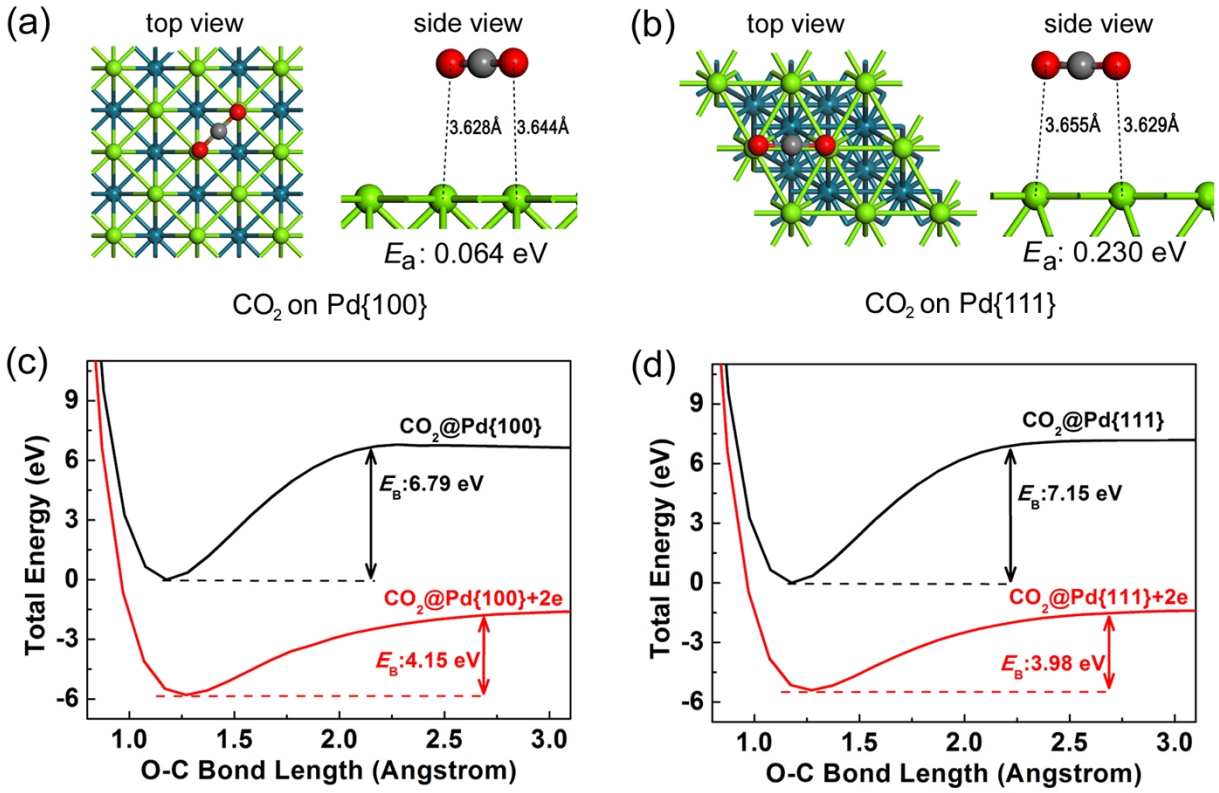

Fig. S20 Optimized configurations for CO_2 adsorbed to (a) Pd{100} and (b) Pd{111} facets together with adsorption energy E_a. Potential energy surface along the O-C bond length for the CO_2 molecule adsorbed to (c) Pd{100} and (d) Pd{111} facets in the neutral state or charged with 2 electrons, from which the CO_2 activation energy E_B is deducted.

Geometry optimizations have spotted four adsorption configurations for CO_2 to Pd{100} or Pd{111} facets (ESI,† Fig. S18 and S19), and the most stable ones (with the highest adsorption energy E_a) have the carbon atom locating on the top of Pd-Pd bond bridge position (ESI,† Fig. S20a and b).

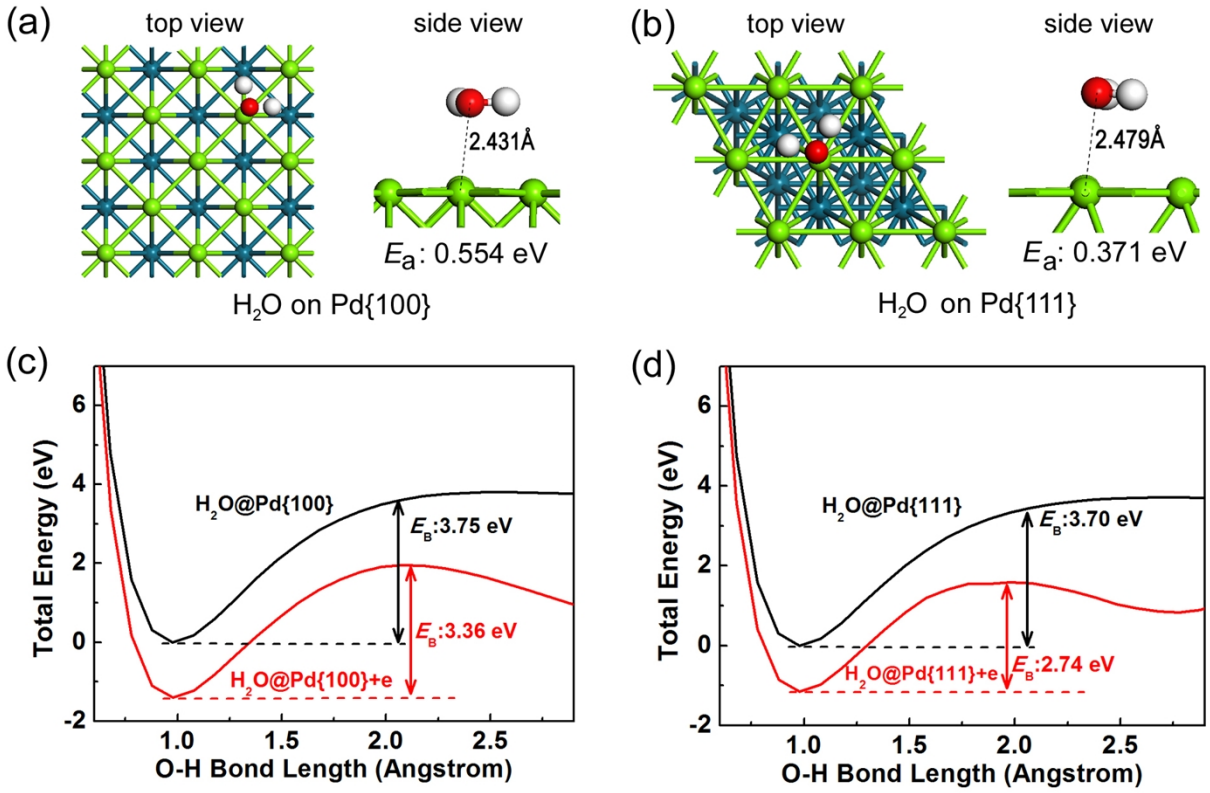

Fig. S21 Optimized configurations for H_2O adsorbed to (a) Pd{100} and (b) Pd{111} facets together with adsorption energy E_a. Potential energy surface along the O-H bond length for the H_2O molecule adsorbed to (c) Pd{100} and (d) Pd{111} facets in the neutral state or charged with 1 electron, from which the H_2O activation energy E_B is deducted.

Note that only the adsorption configuration in ESI,† Fig. S21 can be stabilized during the geometry optimizations for the H_2O molecules.

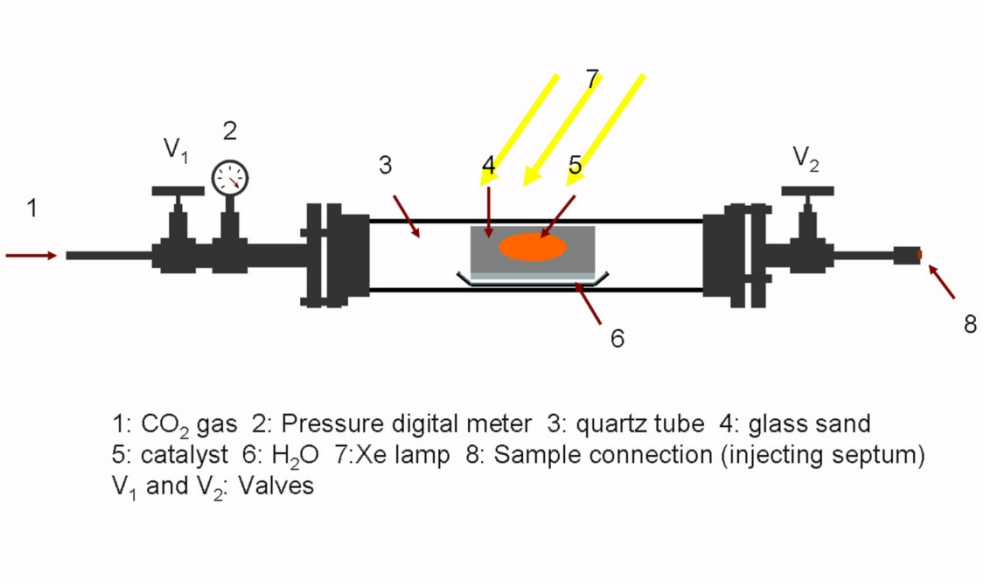

Fig. S22 Schematics illustrating the set-up of photocatalytic system.

Table S1. Product yields of C_3N_4-based photocatalysts for CO_2 reduction in 4 h.

catalyst	product yield (μmol g_{cat}^{-1})			
	H_2	CO	C_2H_5OH	CH_4
bulk C_3N_4	6.8	0.4	0.9	n.d.[b]
C_3N_4 nanosheets	9.2	2.8	1.6	n.d.
C_3N_4-Pd nanocubes[a]	136.4	19.6	2.7	n.d.
C_3N_4-Pd nanotetrahedrons[a]	38.8	81.2	8.7	1.1

[a] Pd loading amounts for the nanocubes and nanotetrahedrons are 5.7 wt% and 5.8 wt%, respectively. [b] Not determined.

References

S1 X. Zhang, X. Xie, H. Wang, J. Zhang, B. Pan and Y. Xie, *J. Am. Chem. Soc.*, 2013, **135**, 18.

S2 C. C. Yang, Y. H. Yu, B. van der Linden, J. C. S. Wu and G. Mul, *J. Am. Chem. Soc.*, 2010, **132**, 8398

S3 G. Kresse and J. Furthmüller, *Phys. Rev. B*, 1996, **54**, 11169.

S4 M. J. Frisch, G. W. Trucks, H. B. Schlegel, G. E. Scuseria, M. A. Robb, J. R. Cheeseman, G. Scalmani, V. Barone, B. Mennucci, G. A. Petersson, H. Nakatsuji, M. Caricato, X. Li, H. P. Hratchian, A. F. Izmaylov, J. Bloino, G. Zheng, J. L. Sonnenberg, M. Hada, M. Ehara, K. Toyota, R. Fukuda, J. Hasegawa, M. Ishida, T. Nakajima, Y. Honda, O. Kitao, H. Nakai, T. Vreven, Jr. J. A. Montgomery, J. E. Peralta, F. Ogliaro, M. Bearpark, J. J. Heyd, E. Brothers, K. N. Kudin, V. N. Staroverov, R. Kobayashi, J. Normand, K. Raghavachari, A. Rendell, J. C. Burant, S. S. Iyengar, J. Tomasi, M. Cossi, N. Rega, J. M. Millam, M. Klene, J. E. Knox, J. B. Cross, V. Bakken, C. Adamo, J. Jaramillo, R. Gomperts, R. E. Stratmann, O. Yazyev, A. J. Austin, R. Cammi, C. Pomelli, J. W. Ochterski, R. L. Martin, K. Morokuma, V. G. Zakrzewski, G. A. Voth, P. Salvador, J. J. Dannenberg, S. Dapprich, A. D. Daniels, Ö. Farkas, J. B. Foresman, J. V. Ortiz, J. Cioslowski and D. J. Fox, *Gaussian 09 Revision A.1* (Gaussian Inc., Wallingford CT, 2009).

S5 Y. Xiong, I. Washio, J. Chen, H. Cai, Z. Y. Li and Y. Xia, *Langmuir*, 2006, **22**, 8563.

S6 X. Wang, K. Maeda, A. Thomas, K. Takanabe, G. Xin, J. M. Carlsson, K. Domen and M. Antonietti, *Nat. Mater.*, 2009, **8**, 76.

S7 S. Yang, Y. Gong, J. Zhang, L. Zhan, L. Ma, Z. Fang, R. Vajtai, X. Wang and P. Ajayan, *Adv. Mater.*, 2013, **25**, 2452.

S8 J. Mao, T. Peng, X. Zhang, K. Li, L. Ye and L. Zan, *Catal. Sci. Technol.*, 2013, **3**, 1253.

S9 H. Xu, J. Yan, X. She, L. Xu, J. Xia, Y. Xu, Y. Song, L. Huang and H. Li, *Nanoscale*, 2014, **6**, 1406.

S10 Y. Xiong, J. Chen, B. Wiley, Y. Xia, Y. Yin and Z. Y. Li, *Nano Lett.*, 2005, **5**, 1237.

S11 S. Sarina, H. Y. Zhu, Q. Xiao, E. Jaatinen, J. Jia, Y. Huang, Z. Zheng and H. Wu, *Angew. Chem. Int. Ed.*, 2014, **53**, 2935.

S12 A. Du, S. Sanvito, Z. Li, D. Wang, Y. Jiao, T. Liao, Q. Sun, Y. H. Ng, Z. Zhu, R. Amal and S. C. Smith, *J. Am. Chem. Soc.*, 2012, **134**, 4393.